

Growth rate and energy dissipation in wind-forced breaking waves

Nicolò Scapin^{1,2}, Jiarong Wu^{1,3}, J. Thomas Farrar⁴, Bertrand Chapron⁵, Stéphane Popinet⁶, and Luc Deike^{1,2}

¹Department of Mechanical and Aerospace Engineering, Princeton University, Princeton, NJ 08544, USA

²High Meadows Environmental Institute, Princeton University, Princeton, NJ 08544, USA

³Courant Institute of Mathematical Sciences, New York University, US

⁴Woods Hole Oceanographic Institution (WHOI)

⁵IFREMER, Univ. Brest, CNRS, IRD, Laboratoire d'Océanographie Physique et Spatiale (LOPS), France

⁶Institut Jean Le Rond d'Alembert, CNRS UMR 7190, Sorbonne Université, Paris 75005, France.

Key Points:

- We perform high-fidelity simulations of wind-forced breaking waves and analyze the wind energy input separating growth and breaking
- Wave growth scales as $(u_*/c)^2$ under wind forcing, with strong amplitude modulation following non-separated sheltering
- Wave breaking triggers turbulence with a z^{-1} dissipation profile, with magnitude controlled by the strength of the breaking event

Abstract

We investigate the energy growth and dissipation of wind-forced breaking waves using direct numerical simulations of the coupled air–water Navier–Stokes equations. We vary the wind friction velocity over the wave speed u_*/c up to 1. A turbulent wind boundary layer drives the growth of a pre-existing narrowband wave field until it breaks and transfers energy into the water column. Under sustained wind forcing, the wave field then resumes growth. We separately analyze energy transfers during wave growth and breaking-induced dissipation. Energy transfers are dominated by pressure input during growth and turbulent dissipation during breaking. The wave growth rate scales with $(u_*/c)^2$, modulated by the wave steepness due to sheltering. The energy dissipation follows the inertial scaling with wave slope at breaking, confirming the universality of the process. Following breaking, near-surface vertical turbulence dissipation profiles scale as z^{-1} , with its magnitude controlled by the breaking-induced dissipation.

Plain Language Summary

Ocean waves grow and eventually break under the action of strong winds, a process that plays a key role in transferring energy from the atmosphere to the ocean and limiting wave heights. In this study, we used high-resolution computer simulations to examine how wind causes waves to grow and how breaking waves transfer energy into ocean currents under high wind speed conditions. Waves grow mainly due to wind pressure on their surface, but once they become steep enough, they break and generate underwater turbulence that carries energy into the ocean. We confirm that the rate at which waves grow and break depends on their steepness and the wind strength. By analyzing the energy lost during breaking, we confirm a universal dissipation pattern that is independent of the specific mechanism leading to breaking. Finally, we propose a new way to describe how this energy distributes below the surface, which agrees well with both our simulations and open ocean field measurements.

1 Introduction

Ocean waves play a critical role in mediating energy transfer between the ocean and the atmosphere. The wind injects energy into the wave field, promoting wave growth and steepening. Once a critical amplitude or velocity is reached, waves break, dissipating part of the energy and transferring it into the water column; contributing to the generation of water currents (Melville and Rapp, 1985), the onset of turbulence in the upper ocean (Lamarre and Melville, 1991; Melville, 1996; Veron and Melville, 2001), and enhanced dissipation in the subsurface currents (Sutherland and Melville, 2015). The characterization of wave growth rates and breaking-induced dissipation in wind waves under strong wind forcing remains an active area of study, with key implications to improve momentum, gas, and energy fluxes formulations in high wind speed regimes such as tropical cyclones and winter storms. The associated momentum and heat fluxes are critical to model tropical cyclone intensification (Sroka and Emanuel, 2021), while the associated energy fluxes and turbulence generation control gas exchange (Deike, 2022) and upper ocean currents (Sullivan and McWilliams, 2010).

Regarding wave growth, two main theories address different stages of the generation mechanism: the early stage, where growth is driven by turbulent pressure fluctuations (Phillips, 1957; Perrard et al., 2019; Li and Shen, 2022), and the finite-amplitude stage, where sufficiently steep waves modulate the atmospheric boundary layer (Jeffreys, 1925; Miles, 1957; Belcher and Hunt, 1993). In the latter regime, the wind input scales with wave energy, theoretically leading to exponential wave growth. Field observations and experimental campaigns have reported several estimates for the growth rate, expressed as a function of the ratio of the wind friction velocity and the wave phase speed u_*/c with significant remaining scatter in the data (Wu et al., 1979; Plant, 1982; Kihara et al., 2007; Grare et al., 2013; Wu et al., 2022). The role of wave steepness modulation at finite amplitudes and the accuracy of the sheltering framework from Belcher and Hunt (1993) using measured wind profiles during wave growth remains to be fully assessed.

The total energy dissipation by wave breaking for individual breaking events (Melville, 1994; Drazen et al., 2008; Banner and Peirson, 2007) has been shown to scale with the wave amplitude at breaking, by extensive laboratory experiments without wind forcing and some limited experiments of wave breaking under wind forcing (Grare et al., 2013). Separately, field observations have discussed

the vertical profile of turbulence dissipation rate and attempted to relate the integrated turbulence beneath an ensemble of breaking waves to the breaking statistics and estimations of the wind input into the wave field (Gemmrich et al., 1994; Craig and Banner, 1994; Terray et al., 1996; Zippel et al., 2022; Sutherland and Melville, 2015; Zippel et al., 2020). Local measurements have reported dissipation rates exceeding classical shear-layer predictions, with the excess attributed to the contribution of breaking events (Terray et al., 1996; Sutherland and Melville, 2015; Zippel et al., 2022; Thomson et al., 2016; Zippel et al., 2020).

In this work, we aim to unify the description of energy transfers, i.e. wind input and energy dissipation, between the wind and growing waves up to the point of breaking. To quantify these processes under strong wind forcing, we perform fully resolved simulations of wind-wave interactions in the presence of wave breaking, building on our previous studies of momentum fluxes (Scapin et al., 2025), and distinguishing between the growing and breaking stages. We use simulations solving the general Navier-Stokes equations for two-phase air-water at high resolution resolving length scales ranging from millimeters to meters, without subgrid models for either wave or turbulence. Such an approach offers direct physical insights into wave breaking that can then be used for the development of subgrid-scale parameterizations in large-scale atmospheric and oceanic models.

This paper is organized as follows. First, in section 2, we discuss the evolution of the water currents, the underwater velocity and dissipation, and how these quantities are affected by wave breaking. Next, in section 3, we extract the wave growth rate directly and quantitatively compare them with Belcher and Hunt (1993), highlighting the mediating role of wave steepness. Then, in section 4, we analyze the breaking-induced dissipation, examining its local behavior during the growing, breaking, and post-breaking stages of the wave field, as well as its global characteristics and confirm the applicability of the inertial scaling from Drazen et al. (2008) in the case of wind-forced breaking waves. We demonstrate that the vertical profiles of turbulence dissipation rate transitions to a $\langle \varepsilon \rangle(z) \propto z^{-1}$ due to breaking, with the level of turbulence dissipation quantified by the inertial scaling, which can also be related to the wind input given the approximate balance between the growing and breaking stages.

2 Direct numerical simulation of wind-forced breaking waves

In this section, we briefly summarize the computational setup in §2.1 already discussed in Scapin et al. (2025), and in §2.2, we describe the evolution of the fully coupled system comprising the wind, wave field, and underwater currents illustrating the velocity and turbulence dissipation rate fields.

2.1 Computational framework

We solve the two-phase air-water Navier-Stokes equations with surface tension using the open-source solver Basilisk (Popinet, 2015; Van Hooft et al., 2018); see also Popinet (2018). A detailed discussion of the numerical setup is provided in Wu et al. (2022); Scapin et al. (2025) and a summary is also provided in the supplementary material. The simulations fully resolve all relevant spatial and temporal scales without sub-grid models or prescribed wave motion. The employed computational domain is a cube of size L_0 , spanning $[-L_0/2, L_0/2]^2 \times [-h_w, h_a]$ and consists of two regions. The upper region Ω_a and height h_a represents the turbulent wind, i.e. a fully-developed turbulent boundary layer, while the lower region Ω_w and depth h_w represents the water currents, with densities (ρ_a, ρ_w) and dynamic viscosities (μ_a, μ_w) , respectively. The computational domain is periodic in the horizontal directions, x and y , while stress-free boundary conditions are applied at the planes $z = -h_w$ and $z = h_a$. The wave field is initialized at the interface Γ using a third-order Stokes wave (Deike et al., 2016; Mostert et al., 2022), with the corresponding irrotational underwater velocity field prescribed according to potential theory (Lamb, 1993; Deike et al., 2015). The fundamental wavelength is denoted by λ .

Following Wu et al. (2022), Scapin et al. (2025) and as also detailed in the supplementary material, the simulation parameters are chosen such that $L_0 = 4\lambda$, $h_a = 3.36\lambda$, and $h_w = L_0 - h_a = 0.64\lambda$, ensuring that the influence of the finite domain size on the wind boundary layer is negligible and that the wave propagation satisfies the deep-water dispersion relation. The air-water density ratio is taken as $\rho_w/\rho_a = 816$. Five remaining non-dimensional groups then govern the problem: the initial wave steepness $a_0 k$ (a_0 the initial amplitude and $k = 2\pi/\lambda$ the wavenumber), the ratio between the friction

Evolution of the wave field during
the first growing G_1 , breaking B_1 and second growing stages G_2

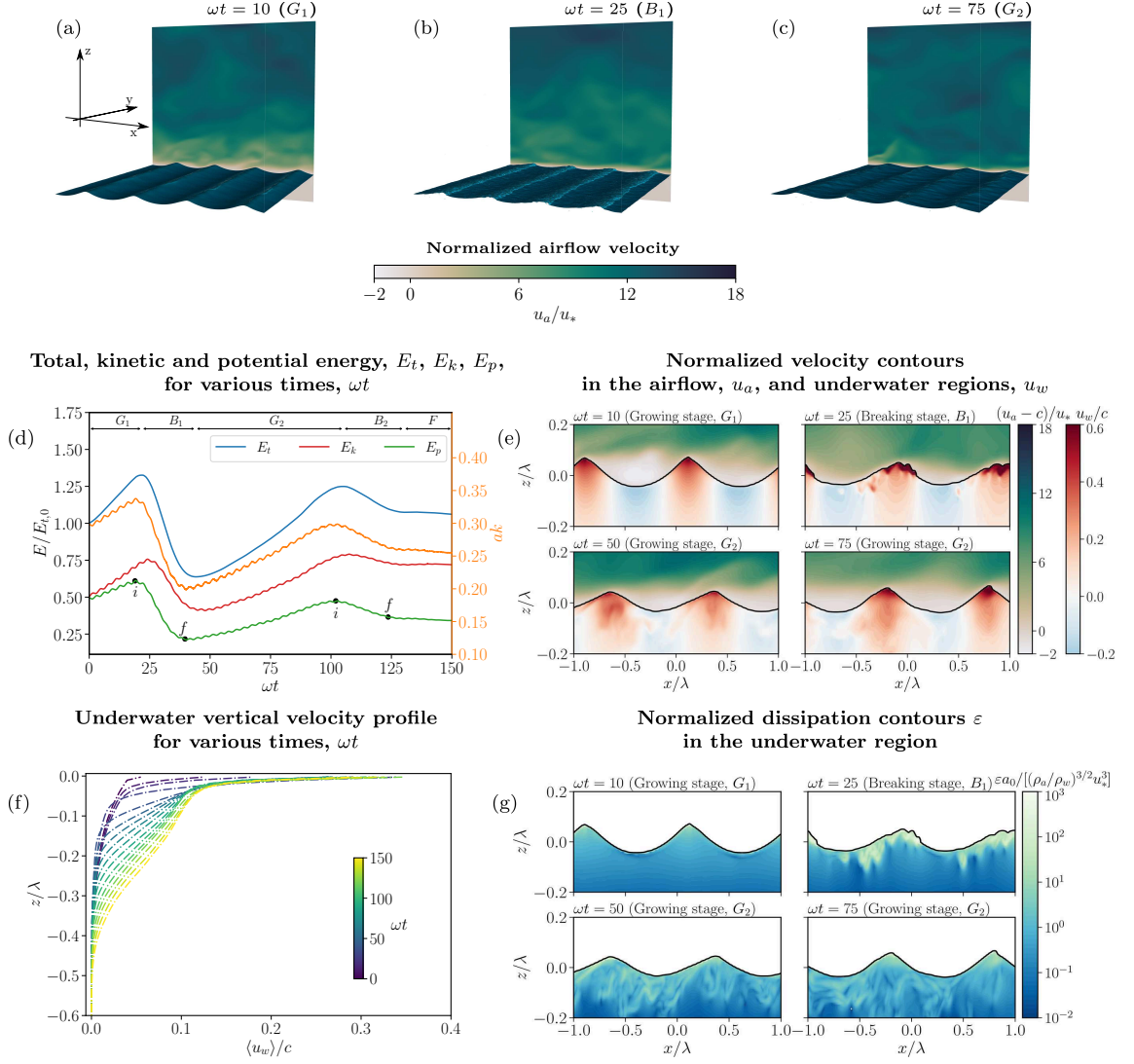


Figure 1: Evolution of the fully coupled airflow, waves, and underwater currents for $u_*/c = 0.9$. The top panels display snapshots illustrating (a) the first growing ($\omega t = 10$, G_1), (b) the breaking ($\omega t = 25$, B_1), and (c) the second growing ($\omega t = 75$, G_2) stages, under turbulent wind forcing which acts parallel to the streamwise direction x . Each panel shows contours of instantaneous streamwise velocity u normalized by u_* . (d) Time evolution of the potential, the kinetic, and total E_p , E_k and $E_t = E_p + E_k$ energy, all normalized by the total initial energy $E_{t,0}$. Equipartition of E_t is lost due to the breaking event. Instantaneous steepness $a(t)k$ is shown on the right axis (orange curve). (e) Instantaneous streamwise velocity on the $y = 0$ plane, normalized by u_* (air) and c (water), across different wave stages. (f-g) For each stage, panel (f) shows the vertical profile of mean streamwise velocity $\langle u_w \rangle$ (averaged along periodic directions) in water, normalized by c , and panel (g) shows dissipation rate $\varepsilon(x, y, z)$ on the $y = 0$ plane, normalized by $(\rho_a/\rho_w)^{3/2}u_*^3/a_0$.

velocity u_* and the wave speed c , i.e. u_*/c , the air and water Reynolds numbers, $Re_{*,\lambda} = \rho_a u_* \lambda / \mu_a$ and $Re_W = \rho_w c \lambda / \mu_w$, which reflects the importance of inertial over viscous forces in the air and in the water. Finally, we have the Bond number $Bo = (\rho_w - \rho_a)g/(\sigma k^2)$, where g is gravity and σ is the surface tension, which represents the importance of gravity over surface tension forces. In particular, we fix $Re_W = 2.55 \cdot 10^4$, $Bo = 200$, and $a_0 k = 0.3$ (ensuring waves are in the gravity regime and that growth to breaking is wind-driven, see Scapin et al. (2025)). We vary u_*/c in the range $[0.3 - 0.9]$, relevant to small-scale processes at high wind speed, such as winter storms and tropical

cyclones (Sroka and Emanuel, 2021). $Re_{*,\lambda}$ is set to 214 to achieve an inertial turbulent regime while keeping the simulation fully resolved and computationally attainable. We also perform a sensitivity analysis at $u_*/c = 0.9$ on both $Re_{*,\lambda}$, exploring values in the range 54.5–107 and the computational domain size, employing a larger domain with $L_0 = 8\lambda$ and $h_a = 6.72\lambda$. These cases will be shown in the following sections, and have a negligible influence on the energy fluxes.

2.2 Development of the underwater currents

In this section, we analyze the development of underwater currents following wave-breaking events, starting from the laminar and irrotational wave initial conditions.

The turbulent wind, propagating in the streamwise direction x and visualized in the first three planes of figure 1, initially promotes the steepening and growth of the wave field, as shown in figure 1(a). Once a critical threshold for breaking is reached, i.e. $(ak)_c \approx [0.28 - 0.33]$ (Banner and Peirson, 1998; Perlin et al., 2013; Deike et al., 2015), the wave field breaks, as shown in figure 1(b). Once this stage is complete, the wave field grows again under wind forcing (fig. 1(c)).

These cycles of growing and breaking stages can be quantified by examining figure 1(d) which reports the wave potential energy E_p , the water kinetic energy E_k and the total energy $E_t = E_p + E_k$ as a function of the dimensionless time ωt ($\omega = 2\pi/T_0$ the angular frequency and $T_0 = \lambda/c$ is the wave period). The kinetic energy is $E_k = \rho_w \int_{\Omega_w} |\mathbf{u}|^2 / 2 dV$, with $\mathbf{u} = (u, v, w)$ the velocity field, and the wave potential energy $E_p = \rho_w g \left(\int_{\Omega_w} z dV - (h_w L_0)^2 / 2 \right)$ (a surface tension contribution to E_t exists but is negligible owing to the large Bond number). Note that the kinetic energy E_k accounts for contributions from mean currents, turbulent fluctuations, and wave motion, while the potential energy E_p is solely associated with the wave field. Both E_k and E_p are shown in figure 1(d), normalized by the initial total energy, $E_{t,0}$, along with an estimate of the wave steepness $a(t)k$, plotted on the secondary y-axis as an orange curve. The wave steepness is estimated either using the amplitude defined as $a(t) = \sqrt{\int_{\Gamma} (2/\Gamma)(\eta - \bar{\eta})^2 d\Gamma}$, where $\eta(x, y)$ is the surface elevation and $\bar{\eta}$ its spatial mean, or from the local slope of the surface, defined as $\max \left(\sqrt{(\partial\eta/\partial x)^2 + (\partial\eta/\partial y)^2} \right)$, and as discussed in Scapin et al. (2025), both approaches were evaluated and yield very similar results.

During the growing phases G_1 - G_2 , E_p increases with time due to wind input. In contrast, during the breaking phases B_1 - B_2 , these contributions decrease as energy is transferred to the water column. As detailed in Scapin et al. (2025), a final stage F is identified, in which the wind input is nearly balanced by energy dissipation. Note that while the potential energy E_p during G_2 is lower than in G_1 due to reduced wave steepness $a(t)k$ as shown by the orange curve in figure 1d), the kinetic energy E_k is higher as a result of the development of underwater currents and the transition to turbulence (which could also influence the growth, as discussed by Kudryavtsev and Chapron (2016)).

Throughout these different stages of the wave field, an underwater velocity current develops. The formation of the current is initially mainly induced by the wind stress (specifically the viscous component), during G_1 , when the underwater flow is still laminar, as shown in the first panel in figure 1(e). However, around $\omega t \approx 20$, the wave breaks, and the associated energy loss is transferred to the water column. The flow field becomes perturbed starting from the wave crest (see the second panel in figure 1(e)), where the local velocity magnitude approaches the wave phase speed. During the breaking event, the flow accelerates and transitions to turbulence during the second growth cycle, as shown in the last two panels of figure 1(e). This transition is also evident in the mean velocity profile $\langle u_w \rangle$ in the water, computed as the spatial average over the x - y plane and plotted using a wave-following coordinate, as described in Wu et al. (2022); Scapin et al. (2025), to capture the dynamics at both the crests and troughs of the wave field (see figure 1(f)). The profile becomes notably steeper, particularly near the wave, i.e., for $z/\lambda < 0.1$. It is important to note that, unlike during G_1 , the velocity currents generated during G_2 are induced not only by wind stress but also by the breaking event, which plays a key role in triggering the transition to turbulence. The use of wave-following coordinates influences the horizontal velocity profile by preferentially sampling regions of higher positive and lower negative velocity—an effect analogous to the origin of Stokes drift (Pollard, 1973). As a result, the velocity profile is not strictly Eulerian, but rather represents an Eulerian–Lagrangian combination. This averaging effect primarily affects mean quantities, while

it is expected to be absent or negligible in the turbulence dissipation rate, as discussed in Wu et al. (2025).

The transition to turbulence in the underwater currents is reflected in the turbulent dissipation, which is computed from the strain rate tensor as

$$\varepsilon(x, y, z) = \nu_w (\partial_i u_j + \partial_j u_i)^2, \quad (1)$$

where $\nu_w = \mu_w / \rho_w$ is the kinematic viscosity of the water. The contours of the dissipation are shown in figure 1(g) and normalized by $(\rho_a / \rho_w)^{3/2} u_*^3 / a_0$, where a_0 is the initial wave amplitude. During the initial growth stage G_1 , ε is nearly negligible and primarily attributed to viscous effects. When the wave breaks during B_1 , dissipation increases but remains localized near the crest. Once the breaking event concludes and the wave field resumes its growth in G_2 , a region of enhanced dissipation (compared to the previous growth cycle, G_1) develops deeper below the wave surface, consistent with the transition of the water currents to turbulence. Having discussed qualitatively the underwater flow during growth and breaking, we will now analyze the energy transfers during each stage.

3 Energy fluxes and growth rate in wind-forced breaking waves

In this section, we study the energy exchanges between the airflow and the wave field: the energy flux due to wind input and the energy dissipation associated with wave breaking. The analysis is done by splitting the growing and breaking stages. In section 3.1, we present the time evolution of the energy flux during the wave growing and breaking stages. In section 3.2, the non-dimensional wave growth rate due to the wind energy flux is discussed and is compared to existing wind growth scaling theories and we demonstrate the importance of the wave slope on growth through sheltering.

3.1 Temporal evolution of the wave energy budget

The energy transfer from the turbulent airflow to the wave field is governed by the evolution of the wave energy, defined as twice the potential energy, i.e., $E_W(t) = 2E_p(t)$, under the assumption of equipartition. As discussed in section 2, equipartition of the total energy E_t between kinetic and potential components (E_k and E_p) is not maintained due to wave breaking. However, we verified that this does not affect the analysis of growth and decay rates, as $dE_W/dt \approx dE/dt$.

The evolution equation for E_W is derived from the action balance equation, a general function of the frequency ω and wave number vector \mathbf{k} , see e.g. Janssen (2004). For a nearly monochromatic wave field evolving over a time scale of $\mathcal{O}(10)T_0$, the dependence of the wave energy E_W on the frequency ω and wavenumber \mathbf{k} can be neglected, as can nonlinear interactions, which do not have sufficient time to develop over such short duration. Under these assumptions, the evolution of the surface-integrated wave energy is given by (Peirson and Garcia, 2008; Grare et al., 2013)

$$\frac{dE_W}{dt} = S_{in} - S_d. \quad (2)$$

In equation (2), S_d is the volume-integrated energy dissipation $S_d = \int_{\Omega_w} \varepsilon(x, y, z) dV$ with $\varepsilon(x, y, z)$ given by eq. (1). The dissipation term S_d incorporates both the viscous effects near the free surface and the energy losses associated with breaking. The loss due to bottom friction (Grare et al., 2013) is negligible for deep water waves.

The wind input S_{in} can be estimated directly from the wave energy, equation (2), as $S_{in} = S_d + dE_W/dt$ as proposed in Donelan et al. (2006); Wu et al. (2022). Separately, the wind input S_{in} can be computed as the surface-integrated energy fluxes contributing to the wave field's growth. It can be decomposed in a pressure $S_{in,p}$ and in a viscous $S_{in,\nu}$ contribution. Following (Grare, L., 2013; Wu and Deike, 2021; Wu et al., 2022), the pressure component can be approximated as the product between the pressure stress and the wave speed, i.e. $S_{in,p} = \tau_{p,x} c$, whereas the viscous component as the product between the viscous stress and the orbital velocity u_o , i.e. $S_{in,\nu} = \tau_{\nu,x} u_o$. From S_{in} , an effective or wave-coherent stress τ_W can be defined as

$$\tau_W = \frac{S_{in}}{c} = \tau_{p,x} + \tau_{\nu,x} \frac{u_o}{c}. \quad (3)$$

Note that equation (3) is based on a linear wave decomposition (using the wave speed and orbital velocity of the wave component), which is valid only during the growing stages. During the breaking

stage, we will estimate the wind input S_{in} using (2), directly based on the time derivative of the wave energy. The viscous contribution during wave growth is negligible as shown in figure 2(a) and as we will observe when comparing both estimates of the wind energy input. The energy budget terms from equation (2) are shown in figure 2(a) for $u_*/c = 0.9$, normalized by the product of the angular frequency ω and the initial wave energy $E_{W,0} = E_W(t = 0)$. The wind input term S_{in} closely matches its pressure component $S_{in,p} \approx \tau_{p,x}c$ during the initial wave growth, consistent with observations by Wu et al. (2022). However, this agreement stops during wave breaking, when the linear wave assumptions used to compute $S_{in,p}$ no longer hold, leading to significant discrepancies between S_{in} and $S_{in,p}$. The viscous contribution $S_{in,\nu}$ remains much smaller than $S_{in,p}$ throughout, with only a slight increase following breaking due to enhanced viscous stress.

The time evolution of the energy budget reported in figure 2(a) for $u_*/c = 0.9$ follows three stages: the first growing cycle, the breaking stage, and the second growing cycle. In the first growing cycle, the accumulation term dE_W/dt and the energy input S_{in} are the dominant terms with a limited contribution of the dissipation term, mainly due to viscous friction. During the second stage, when the wave field breaks, S_{in} becomes negative, and the wave stops absorbing energy from the airflow as its energy decreases because of the loss of coherence between the air-flow pressure field and the breaking wave. During breaking, the dissipation S_d increases and becomes the dominant positive term in the wave energy budget, as the potential wave energy is transferred into turbulent kinetic energy in the water column. During the second growing cycle, the wind input (evaluated directly or from the pressure) is positive again but lower than the value in the first growing cycle due to the reduced ak and associated reduced form drag. Furthermore, during the second growing stage, the dissipation is reduced compared to the breaking event but larger than the first growing cycle since the water beneath the wave is turbulent, and the bulk dissipation is enhanced, as discussed in section 2.2.

3.2 Comparison of the growth rate to existing theoretical framework

We now aim to quantitatively predict the wave growth rate of the waves due to the wind input. The wind input is used to estimate the instantaneous, non-dimensional wave growth rate, defined as (Belcher and Hunt, 1993; Belcher, 1999)

$$\gamma(t) = \frac{S_{in}(t)}{\omega E_W(t)}, \quad (4)$$

where $S_{in}(t)$ is the wind energy input, ω the angular frequency, and $E_W(t)$ the wave energy. The non-dimensional wave growth rate, $\gamma(t)$, can be evaluated in an averaged sense, denoted as $\bar{\gamma}$, over the growing stages G_1 and G_2 . The averaged growth rate $\bar{\gamma}$ can then be compared with theoretical frameworks that describe its dependence on wave parameters, particularly the wave slope ak and the normalized friction velocity u_*/c .

Following Peirson and Garcia (2008); Melville and Fedorov (2015); Buckley et al. (2020), and relating the wind input to the product of the wave phase speed and the wave-coherent momentum flux, i.e. $S_{in} = c\tau_W$, together with using $E_W = \rho_w g a^2/2$ and the dispersion relation $c = \sqrt{g/k}$, the time-averaged, non-dimensional growth rate can be expressed as

$$\bar{\gamma} = \frac{2\tau_W}{\rho_w c^2 a k^2}. \quad (5)$$

Following equation (6), finding the non-dimensional growth rate $\bar{\gamma}$ for a wind and wave condition reduces to finding the wave-coherent momentum flux τ_W defined in equation (3). Earlier theories summarized in Kihara et al. (2007); Wu et al. (2022) based on sheltering Jeffreys (1925), and critical layer Miles (1957) lead to $\tau_W = \alpha_p (\bar{a}k^2/2) \rho_a u_*^2$, with α_p function of the wind structure and wave slope, or assumed to be a constant, leading to the classic form for $\bar{\gamma}$

$$\bar{\gamma} = \frac{\rho_a}{\rho_w} \alpha_p \left(\frac{u_*}{c} \right)^2. \quad (6)$$

In the present configuration, for high values of u_*/c and steep waves, the critical layer, i.e. the height where $\langle u \rangle(z) = c$, lies within the viscous sublayer, where the assumptions behind Miles' original theory, particularly the inviscid and quasi-laminar approximations, no longer hold. Although later extensions (Miles, 1959) attempt to incorporate viscous effects, they still rely on the quasi-laminar

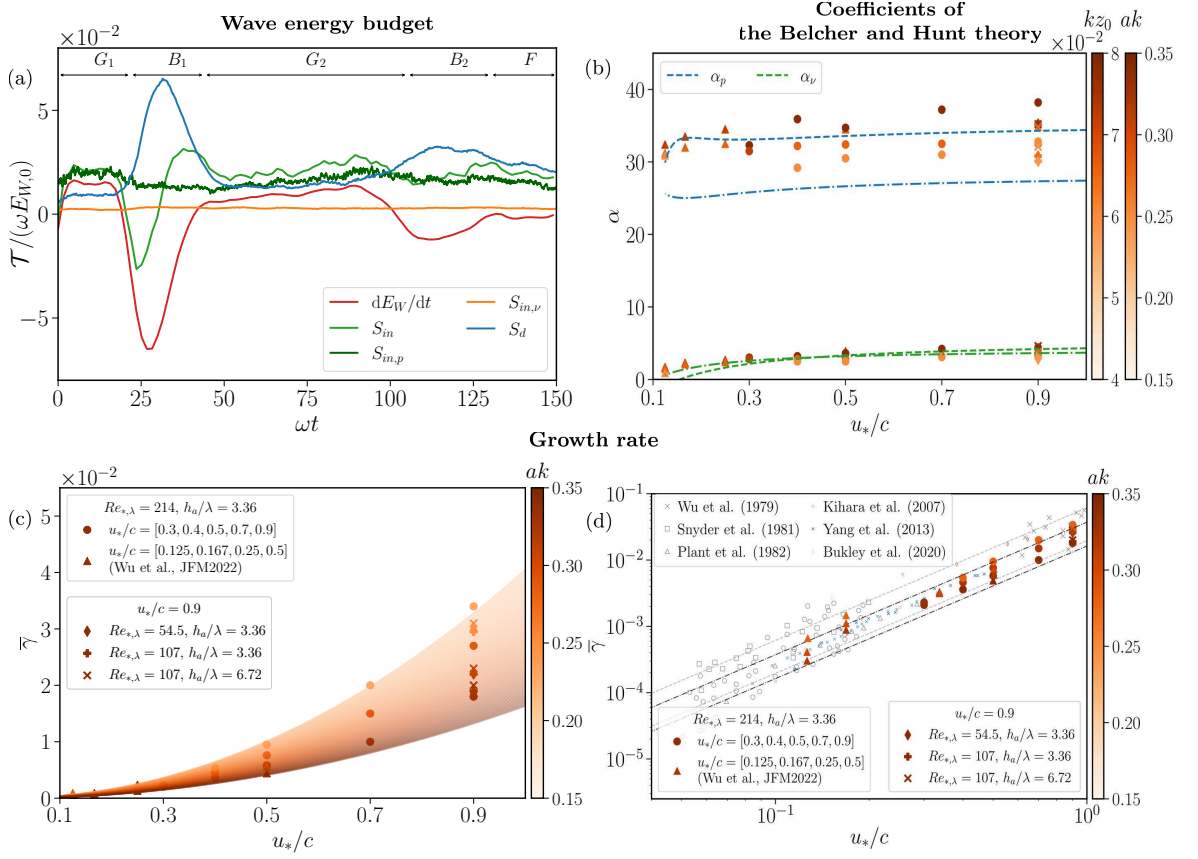


Figure 2: (a) Wave energy budget terms (see equation (2)) for $u_*/c = 0.9$. The y-axis shows $\mathcal{T} = dE_W/dt$, total wind input S_{in} , and dissipation ε , each time-dependent and normalized by $\omega E_{W,0}$, where $\omega = \sqrt{gk}$ and $E_{W,0} = E_W(t = 0)$. The dark green curve denotes the pressure wind input, $S_{in,p} = \tau_{p,x}c$, and the orange curve denotes the viscous pressure input, $S_{in,\nu}$. (b) Variation of the coefficients α_p and α_ν of the Belcher and Hunt theory for multiple ak and for different u_*/c . Each case includes one point from the first growth and two points from two windows in the second growth. Dashed and dot-dashed curves show isolines at fixed surface roughness $kz_0 = 6 \cdot 10^{-3}$ and $6 \cdot 10^{-2}$, using equations (10), (11) and $\langle u \rangle = (u_*/\kappa) \log(z/z_0)$. Two colorbars indicate kz_0 and ak . (c-d) Variation of $\bar{\gamma}$ as a function of u_*/c . The shaded area shows estimates from equation (9) using $\bar{\alpha}_p = 31.4$ and $\bar{\alpha}_\nu = 4.6$ for $ak \in [0.15, 0.33]$. In both (c) and (d), *up triangles* show present data; *circles*, data from (Wu et al., 2022). In (d), we show the theoretical prediction using equation (9) using $\bar{\alpha}_p$ and $\bar{\alpha}_\nu$ for values for minimum and maximum ak (black dot-dashed lines), the estimations from Plant (1982) (gray dashed lines) and additional datasets noted in the legend.

assumption and neglect wave-induced turbulence, which becomes important for steep waves. Belcher and Hunt (1993) relaxes these assumptions and accounts for pressure perturbations arising from turbulent sheltering—i.e., asymmetric distortion of turbulent eddies by the wave, which remains effective even when the critical height lies within the roughness or viscous sublayer. Belcher and Hunt (1993); Belcher (1999) then theoretically compute the wave-coherent momentum flux τ_W under such assumptions. They separate the turbulent boundary layer into an inner and an outer region. In the inner region, which is close to the wave surface, turbulent eddies are assumed in equilibrium with the mean velocity gradient, and the characteristic timescale for the eddy to decorrelate and interact with another one is $T_L = \kappa\eta/u_*$. The turbulence flow here can be fairly described with a mixing-length model (Townsend, 1951). In the outer region, turbulent eddies are rapidly distorted by the flow with a timescale $T_A = k/[\bar{u}(\eta) - c]$, the turbulence flow can be better described using the rapid distortion theory (Belcher and Hunt, 1993). Under the assumption of negligible flow separation (i.e. non-separated sheltering) over the wave surface, (Belcher and Hunt, 1993) employed formal asymptotic expansions to evaluate the surface pressure and viscous stress distribution. The relations

were then employed to directly compute $\tau_{W,p}$ and $\tau_{W,\nu}$ as

$$\tau_{W,p} = \frac{\alpha_p \overline{ak}^2 / 2}{1 + \alpha_p \overline{ak}^2 / 2} \rho_a u_*^2, \quad (7)$$

$$\tau_{W,\nu} = \frac{\alpha_\nu \overline{ak}^2 / 2}{1 + \alpha_p \overline{ak}^2 / 2} \rho_a u_*^2, \quad (8)$$

where the terms α_p and α_ν are the pre-factors of the pressure and viscous stress momentum fluxes that can be explicitly calculated with knowledge of the wind profile. By substituting equations (7) and (8) into (6), the non-dimensional wave growth rate can be expressed as

$$\bar{\gamma} = \frac{\rho_a}{\rho_w} \frac{2(\alpha_p + \alpha_\nu)}{2 + \alpha_p \overline{ak}^2} \left(\frac{u_*}{c} \right)^2. \quad (9)$$

Note that eq. (9) contains the explicit dependence on the wave steepness \overline{ak} . For negligible viscous stress work, i.e. $\alpha_\nu \ll \alpha_p$, and for 'small' \overline{ak} , i.e. $\overline{ak} \lesssim 0.15$, $\tau_{W,p} \approx \alpha_p (\overline{ak}^2 / 2) \rho_a u_*^2$, equation (9) reduces to eq. (6) from (Miles, 1957; Jeffreys, 1925).

The framework developed in Belcher (1999) provides a closed expression for α_p and α_ν which read as follows

$$\alpha_p = 2 \left(\frac{\langle u \rangle_m - c}{\langle u \rangle_i - c} \right)^4 \left(2 - \frac{c}{\langle u \rangle_i} \right) - 2 \left(\frac{\langle u \rangle_m - c}{\langle u \rangle_i - c} \right)^2 \frac{c}{\langle u \rangle_i} + 2\kappa \delta^{2n} \left(\frac{\langle u \rangle_m - c}{u_*} \right), \quad (10)$$

$$\alpha_\nu = \frac{2(\langle u \rangle_m - c)^2}{(\langle u \rangle_i - c)u_i} - \frac{2c}{\langle u \rangle_i}. \quad (11)$$

In equations (10) and (11), the velocities $\langle u \rangle_m$ and $\langle u \rangle_i$ correspond to the streamwise velocity field evaluated at the two vertical positions in the boundary layers, z_i and z_m . Here, z_i is the height in the boundary layer at which $T_A = T_L$, z_i can be computed iteratively from the equation $kz_i |\log(z_i/z_0) - \kappa c/u_*| = 2\kappa^2$, while z_m is a mid-layer height $kz_m = (\delta/\kappa)^{0.5}$ with $\delta = u_*/|u(\lambda/2\pi)|$ (Belcher and Hunt, 1993). It is important to remark that the expressions in equations (10) and (11) reduce the calculation of τ_W and $\bar{\gamma}$ to the evaluation of the streamwise velocity profile at three different heights in the airflow region, i.e. $z = [z_i, z_m, \lambda/2\pi]$.

Here we extract the pre-factors α_p , α_ν directly from the velocity profiles evaluated from the DNS (profiles are shown in Scapin et al. (2025)), shown in Figure 2(b) for different values of u_*/c . Data point colors indicate different instantaneous \overline{ak} values corresponding to the mean \overline{ak} during the first growing cycle, and from equally sized averaging windows in the second growing cycle, which features two distinct \overline{ak} values.

We note that when considering a log-layer to describe the mean wind profile $\langle u \rangle = (u_*/\kappa) \log(z/z_0)$, the pre-factors α_p and α_ν can then be evaluated from the values of u_*/c and an estimation of the surface roughness z_0 , as discussed in Belcher and Hunt (1993); Belcher (1999). For the range of u_*/c investigated in this work ($u_*/c \in [0.125, 0.9]$), the pre-factors $\alpha_{p,\nu}$ obtained from our DNS exhibit limited sensitivity to variations in u_*/c , but show a clearer dependence on the surface roughness length z_0 . In particular, $\alpha_{p,\nu}$ decreases with decreasing kz_0 , which corresponds to a reduction in the instantaneous steepness ak . However, since the range of kz_0 covered in our simulations is relatively narrow ($kz_0 \in [4 \cdot 10^{-2}, 8 \cdot 10^{-2}]$), the resulting variation in $\alpha_{p,\nu}$ remains moderate. Furthermore, the pressure contribution to α_p is significantly larger than the viscous contribution α_ν , with the ratio α_ν/α_p increasing from approximately 0.04 at low u_*/c to about 0.12 at the highest u_*/c considered.

Given the limited variability of $\alpha_{p,\nu}$ over the investigated parameter space, it is appropriate to represent them using single mean values in the following. Based on figure 2(b), we adopt $\bar{\alpha}_p = 31.4$ and $\bar{\alpha}_\nu = 4.6$. These values are employed to compute the growth rate using equation (9) for different values of steepness in the range reached during the different cases $ak \in [0.15 - 0.35]$. The results are reported in figure 2(c), where we compare the predictions using (9) with the data points extracted from the DNS. Figure 2(c) clearly shows the modulation of $\bar{\gamma}$ induced by wave steepness for a fixed u_*/c and emphasizes the importance of its inclusion in the expression of wave-coherent stresses and the growth rate.

Figure 2(d) combines the estimation of $\bar{\gamma}$ from our DNS, the ones retrieved from (Wu et al., 2022) at lower u_*/c and a collection of numerical and experimental data (Wu et al., 1979; Snyder et al., 1981; Plant, 1982; Kihara et al., 2007; Yang et al., 2013; Buckley et al., 2020). Furthermore, we include the estimation of the theoretical growth rate following (9) (black dot-dashed) with $\bar{\alpha}_p = 31.4$, $\bar{\alpha}_\nu = 4.6$ for $ak_{\min} = 0.15$, $ak_{\max} = 0.35$, and the one obtained in Plant (1982) (grey dashed lines), who suggested $\gamma = (0.04 \pm 0.02)(u_*/c)^2$ (equation (6)).

As discussed in previous studies, there is a large scatter in the values of $\bar{\gamma}$ at a given u_*/c , reaching up to one order of magnitude. This can be attributed to several factors. First, the estimation of the wind input S_{in} is subject to significant uncertainty due to the challenges associated with measuring aerodynamic pressure (Grare et al., 2013). Second, additional uncertainty stems from the dependence on the wind velocity profile and the lack of direct measurements of such profiles. Reported values of the coefficients, fitted from observed growth rates, i.e. using equation (6) to retrieve α_p , as done in Peirson and Garcia (2008) - vary by up to an order of magnitude (Belcher, 1999). The framework developed by Belcher and Hunt (1993) provides a physical approach to evaluate $\alpha_{p,\nu}$ based on knowledge of the wind profile and highlights the modulation of the growth rate by the wave slope as a source of scatter in the growth rate at a given u_*/c . In the regime probed here of high values of u_*/c and slope ak , the critical height becomes located too close to the surface in the surface layer, and a sheltering approach such as the one from Belcher, incorporating the effect of turbulence, becomes preferable.

4 Wave breaking-induced dissipation

In this section, we discuss the turbulence dissipation induced by wave breaking. First, in section 4.1, we confirm that the dissipation caused by wave breaking is controlled by the wave slope at breaking and is quantified by the inertial scaling originally proposed by Drazen et al. (2008). Next, in section 4.2, we analyze the vertical profiles at different stages of the wave field and demonstrate that wave breaking promotes a transition to turbulence, with $\langle \varepsilon \rangle(z) \propto z^{-1}$, and demonstrate that the inertial scaling argument for the dissipation due to breaking can be used to unify the dissipation profiles at different u_*/c .

4.1 Estimation of the breaking parameter

In this section, we characterize the breaking stage of the wave field and, in particular, compare the energy loss observed during the wind-forced breaking events simulated here with previous results obtained in the absence of wind forcing. We also examine the applicability of the inertial scaling laws proposed for plunging and spilling breakers (Drazen et al., 2008; Pizzo and Melville, 2013). The comparison includes data from laboratory experiments (Banner and Peirson, 2007; Drazen et al., 2008; Grare et al., 2013) and numerical simulations (Deike et al., 2016; De Vita et al., 2018; Mostert et al., 2022).

The inertial scaling law of Drazen et al. (2008) adapts the classical turbulent dissipation scaling (Taylor, 1938; Vassilicos, 2015) to wave breaking. The local dissipation rate is estimated using Taylor's frozen turbulence hypothesis, i.e. $\varepsilon = C_\varepsilon w_c^3/h_c$, with $C_\varepsilon = \mathcal{O}(1)$, $h_c = a$ the breaking height, and $w_c = \sqrt{2ga}$ the ballistic velocity (Drazen et al., 2008). The breaking-induced turbulence is assumed confined to a volume AL_c , where $A \approx \pi a^2/4$ (Duncan, 1981; Drazen et al., 2008) and L_c is the crest length. Note that $L_c = 4\lambda$ in our setup. The dissipation per unit crest length is then $\varepsilon_l = \varepsilon/L_c = \rho_w \varepsilon A$ (Duncan, 1981; Phillips, 1985; Deike, 2022). Using the dispersion relation, this leads to $\varepsilon_l = b \rho_w c^5/g$, where $b = \chi_0 S^{5/2}$, $\chi_0 = (\pi/\sqrt{2})C_\varepsilon$, and $S = (ak)_c$ is the breaking slope. Introducing a threshold slope $S_0 \approx 0.08$ (Romero et al., 2012; Grare et al., 2013), the final form is

$$b = \chi_0 (S - S_0)^{5/2}. \quad (12)$$

We can now compare the energy decay rate extracted by our DNS with the one estimated from the inertial scaling. To estimate the breaking parameter b , we consider the temporal variation of the potential energy $E_W = 2E_p$ reported in 1(c) for $u_*/c = 0.9$. Here, we define two physical times, t_i and t_f , as the initial and the final physical times when the breaking event starts and ends, respectively, and evaluate $\varepsilon_l = 2(E_{p,i} - E_{p,f})/(L_c(t_i - t_f))$, where $E_{p,i}(t = t_i)$ and $E_{p,f}(t = t_f)$ are defined as $E_{p,i} = \max(E_p)$ and $E_{p,f} = \min(E_p)$ and are evaluated over a single growing/breaking cycle. This procedure is applied for the remaining cases at different u_*/c .

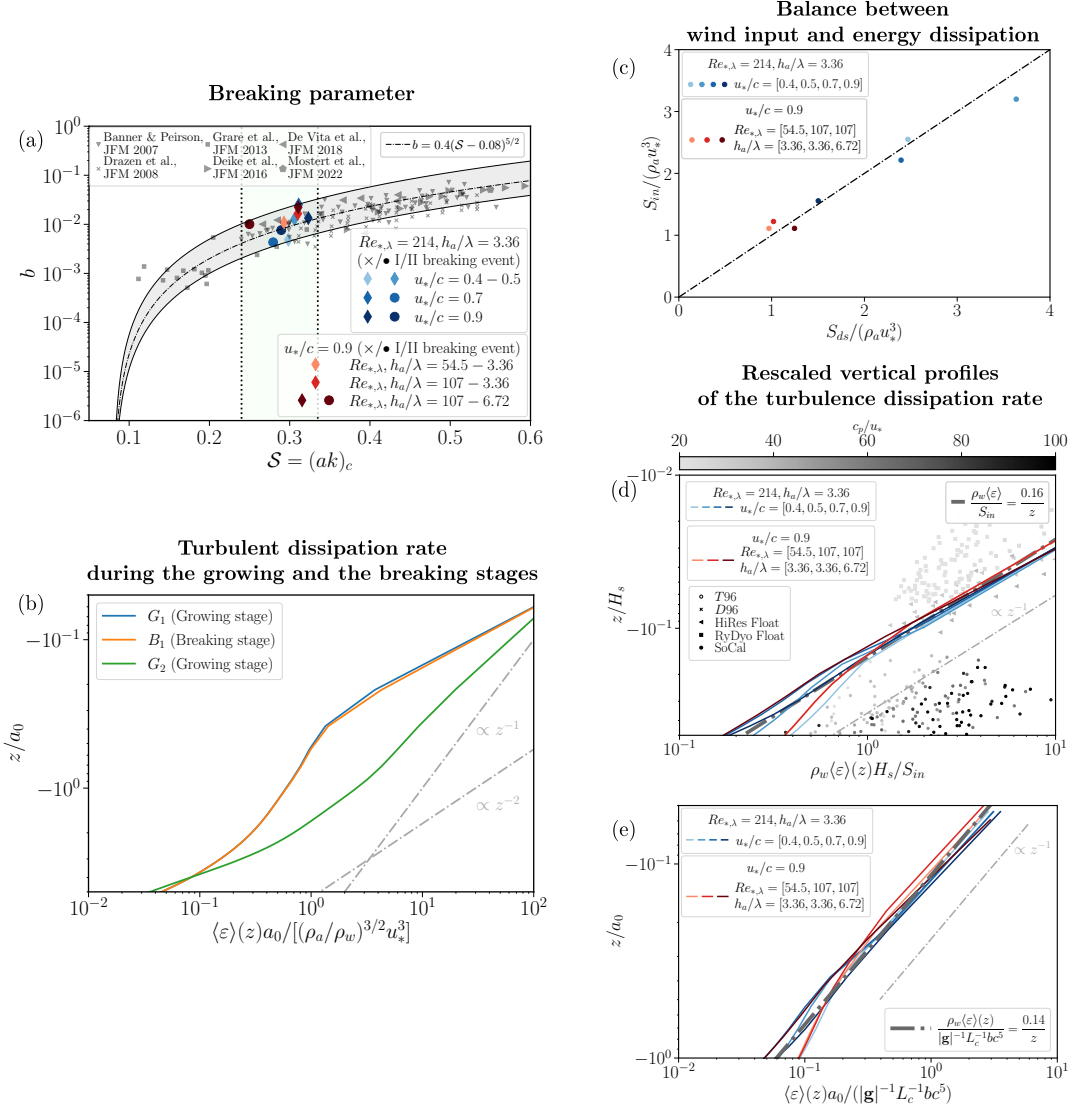


Figure 3: (a) Breaking parameter b as a function of wave steepness for various u_*/c values. Solid lines show estimates from equation (12) with $\chi_0 = 0.25 - 0.95$, vertical dot-dashed lines mark the breaking range in our simulations, $(ak)_c = 0.28 - 0.33$, black dot-dashed line the estimation of $b = 0.4(S - 0.08)^{5/2}$ (Deike et al., 2016). For $u_*/c = 0.7-0.9$, b is shown for both first and second breaking events. Experimental data with/without wind (Banner and Peirson, 2007; Drazen et al., 2008; Grare et al., 2013) and DNS without wind forcing (Deike et al., 2016; De Vita et al., 2018; Mostert et al., 2022) are also shown. (b) Time-averaged dissipation profiles for $u_*/c = 0.9$ during first growth (G_1), first breaking (B_1), and second growth (G_2), normalized by $(\rho_a / \rho_w)^{3/2} u_*^3 / a_0$. (c) Normalized wind input $S_{in} = \tau_{W,p} c$ as a function of the breaking-induced dissipation $S_{ds} = \rho_w g^{-1} L_c^{-1} b c^5$. (d) Dissipation profiles after breaking (G_2), normalized by H_s to compare with the field data from Terray et al. (1996); Drennan et al. (1996); Sutherland and Melville (2015), where wind input is estimated from a spectral parameterization. (e) Depth normalized by a_0 and dissipation normalized by $S_{ds} / (\rho_w a_0)$.

The results are reported in figure 3(a), compared to laboratory experiments on wave breaking (Banner and Peirson, 2007; Drazen et al., 2008) and the scaling $b \sim S^{5/2}$ with a range of the scaling pre-factor χ_0 , (of order $\mathcal{O}(1)$) from $\chi_0 \in [0.25 - 0.95]$, as suggested in the literature, by experimental and numerical data (Romero et al., 2012; Deike et al., 2015; Mostert et al., 2022; Deike et al., 2016). The DNS data of breaking forced at high wind speed agree well with the theoretical scaling and the laboratory experiments for the full range of tested u_*/c .

We conclude that the scaling $b \propto \mathcal{S}^{5/2}$, originally developed for breaking waves without wind input (Melville, 1994; Drazen et al., 2008) applies in the context of wind-forced breaking waves. This observation confirms that the breaking event appears to be a universal process, with its decay rate remaining largely independent of the specific cause triggering the event, such as wind input, and solely dependent on the amplitude at breaking. In practice, using the breaking height a as characteristic length and $\sqrt{2ga}$ as characteristic velocity, the breaking-induced dissipation is determined by a unique parameter b for breaking waves induced by linear and non-linear focusing, as well as wind-forced (Iafrafi, 2009; Deike et al., 2015; De Vita et al., 2018; Deike et al., 2016; Mostert et al., 2022; Grare et al., 2013; Drazen et al., 2008; Melville, 1994; Banner and Peirson, 2007).

4.2 Vertical profiles of the dissipation

In this section, we examine the vertical distribution of turbulent dissipation. The local dissipation rate, computed using equation (1), is averaged over the two periodic directions, yielding the mean profile as a function of depth $\langle \varepsilon \rangle(z)$. Following Wu et al. (2022); Scapin et al. (2025), the profiles are plotted using a wave-following coordinate system to ensure that the spatial averaging accounts for both the crests and troughs of the wave field.

Figure 3(b) shows the dissipation profile normalized by $(\rho_a/\rho_w)^{3/2}u_*^3/a_0$ as a function of water depth z normalized by a_0 , for the case $u_*/c = 0.9$. The three profiles are time-averaged over the first growing and breaking stages, i.e. G_1 - B_1 , and during the second growing cycle, G_2 . We observe that the dissipation profile becomes steeper and approaches the z^{-1} scaling, a transition attributed to wave breaking during stage B_1 . Notably, during this stage, the regions of high dissipation remain confined near the wave field, but in the subsequent post-breaking stage G_2 , they propagate down to a water depth of approximately $5a_0$ (also visible in figure 1(g)). Below this depth, the magnitude of turbulence dissipation becomes negligible.

Under strongly forced wind conditions, characterization of the wave spectra, breaking distribution and associated upper ocean turbulence have often invoked the assumption of equilibrium between the energy input from the wind S_{in} and the total dissipation due to breaking S_{ds} (Phillips, 1985; Drennan et al., 1996; Terray et al., 1996; Sutherland and Melville, 2015; Zippel et al., 2020; Wu et al., 2025; Zippel et al., 2022; Wu et al., 2023).

We can directly assess the balance between wind input (evaluated during the growth stage) and energy dissipation (evaluated during the breaking stage) in the present set-up. Figure 3(c) shows the wind input S_{in} extracted directly from the DNS (during the growth stage) as a function of the total dissipation S_{ds} , evaluated from the DNS (during the breaking stage) as $S_{ds} = \rho_w g^{-1} \int b \Lambda(c) c^5 dc$ (the fifth moment of the breaking distribution $\Lambda(c)$, following Duncan (1981); Phillips (1985)), which simplifies to $S_{ds} = \rho_w g^{-1} L_c^{-1} b c^5$ in our narrowbanded wave conditions. The balance between both terms (S_{in} and S_{ds}) happening subsequently in time is well observed.

To compare results across different wind conditions, Terray et al. (1996); Drennan et al. (1996); Sutherland and Melville (2015) presented the vertical profiles of turbulence dissipation rate $\langle \varepsilon \rangle(z)$ normalized by the wind input S_{in} , using the significant wave height H_s as characteristic vertical height. Such normalization is shown in figure 3(d), alongside field data from Sutherland and Melville (2015). The numerical profiles of $\rho_w \langle \varepsilon \rangle(z) H_s / S_{in}$ exhibit an excellent collapse up to $0.1 H_s$, maintaining a z^{-1} scaling and are well described by

$$\langle \varepsilon \rangle(z) = A \frac{S_{in}/\rho_w}{z}, \quad (13)$$

where $A \approx 0.16$ is a non-dimensional constant obtained by best fit to the data. The numerical data falls within the scatter of the field observations. Note that in our fully resolved setup, the water-side Reynolds number is high enough for dissipation to become Reynolds-independent (Mostert et al., 2022), though still significantly lower than in field conditions, where enhanced dissipation extends up to H_s (Sutherland and Melville, 2015; Wu et al., 2025). We note that the validity of the scaling in equation (13) is inconsistent with the wall-layer scaling for dissipation, $\langle \varepsilon \rangle_{wl}(z) = u_{*,w}^3/(\kappa z)$, with $u_{*,w} = u_*(\rho_a/\rho_w)^{1/2}$ the friction velocity in water and $\kappa = 0.41$ the von Kármán constant, which has sometimes been discussed as a default scaling for $\langle \varepsilon \rangle(z)$. Indeed, equation (13) implies $\langle \varepsilon \rangle(z) \sim u_*^2 c/z$ since $S_{in} \sim u_*^2 c$, while the wall-layer scaling suggests $\langle \varepsilon \rangle(z) \sim u_*^3/z$. Therefore, the physical argument behind the wall-layer scaling (based on shear-induced turbulence) is not appropriate for characteriz-

ing the dissipation profiles below breaking waves at different values of u_*/c (see the supplementary material).

Since we have observed the balance $S_{in} \approx S_{ds}$ (figure 3(c)), we expect that normalizing the dissipation profile by the dissipation due to wave breaking S_{ds} will unify the profiles across different u_*/c . The results are shown in figure 3(e), where we observe a good collapse of the turbulence dissipation profiles across different values of u_*/c when rescaled using S_{ds} . The vertical turbulence dissipation profiles are well described by

$$\langle \varepsilon \rangle(z) = \mathcal{A} \frac{S_{ds}/\rho_w}{z} = \mathcal{A} \frac{g^{-1} L_c^{-1} b c^5}{z}. \quad (14)$$

with $\mathcal{A} \approx 0.14$ a non-dimensional constant obtained by best fit to the data, which has a very similar value to A in equation (13). The underwater dissipation is fully described by the breaking parameter b (function of the wave slope at breaking) and the wave speed c in a way fully consistent with the inertial scaling from Drazen et al. (2008) and the original description of dissipation by breaking from Duncan (1981); Phillips (1985).

It is worth commenting that the observed scaling of dissipation profiles with either wind input, as described by equation (13) and shown in figure 3(d), and with total dissipation due to breaking, as per equation (14) and displayed in figure 3(e), is fully consistent with our understanding of wind-wave growth (here using the sheltering idea) and dissipation by breaking (given by the inertial scaling argument discussed) combined with the idea of balance between wind input and breaking induced dissipation. Wave breaking fundamentally arises from fluid inertia overcoming restoring forces such as gravity and surface tension. After the onset of breaking, wind input no longer directly influences the dissipation rate. However, the total energy transferred from the wind to the wave field is critical, as it governs the conditions under which breaking occurs. Therefore, it is coherent that the underwater turbulence dissipation scales both with the total wind energy input via equation (13) and with the local steepness at breaking via equation (14) under conditions of local equilibrium.

5 Conclusions

We performed direct numerical simulations of wind-forced breaking waves in a high wind speed regime, capturing the wind-driven growth of a narrowband wave field up to the onset of breaking, followed by energy dissipation due to breaking and the resulting underwater turbulence structure. Building upon our previous work (Scapin et al., 2025), we divide the overall evolution of the wave field into two distinct stages, i.e. growth and breaking, and analyze each sub-process separately.

First, we confirm that during the growing stage, wave growth is primarily driven by pressure drag. During the breaking stage, the energy loss from the wave field becomes the dominant mechanism of energy transfer to the water column, further accelerating the development of underwater drift and promoting the transition to turbulence in the subsurface currents. This, in turn, enhances turbulence dissipation in the underwater flow. We quantify the wave growth rate and show that the growth is strongly modulated by the wave steepness, which contributes to the variability in growth rate estimates at the same u_*/c observed in the literature.

During wave breaking, we measure the energy loss and demonstrate that it follows the inertial scaling law $b \sim S^{5/2}$, consistent with prior experiments and simulations conducted in the absence of wind forcing. This confirms that the energy loss is primarily governed by the wave amplitude at the onset of breaking and is insensitive to wind input.

Finally, we examine energy dissipation and show that, following breaking events, vertical dissipation profiles exhibit a clear z^{-1} scaling near the surface, in agreement with field observations. When normalized by the wind input S_{in} , these profiles collapse across a wide range of friction velocity ratios u_*/c , supporting the idea that the dimensionless group $\rho_w \langle \varepsilon \rangle H_s / S_{in}$ is an appropriate scaling to characterize near-surface turbulence generated by breaking waves. Moreover, we observe a balance between wind input (evaluated during growth) and energy dissipation (during breaking), supporting the assumption that the total wind energy input is transferred to the water column via breaking. Building on this, we propose a rescaling of the dissipation profiles using the fifth moment of the breaking distribution, expressed as $\langle \varepsilon \rangle = \mathcal{A}(g^{-1} L_c^{-1} b c^5)/z$, which explicitly includes the breaking

parameter b and wave speed c . This new scaling law also yields an excellent collapse of the dissipation profiles across different values of u_*/c .

Overall, our results confirm that wave breaking, which arises when fluid inertia overcomes restoring forces, is a universal process whose associated energy loss and turbulence generation are largely independent of the specific mechanism that triggers the event. These findings offer new insights into the physical processes governing air-sea energy exchange under strong wind forcing with implications for the development of new physics-based parameterizations of momentum and energy fluxes in high wind speed regimes relevant to tropical cyclones and winter storms.

Open Research Statement

The Basilisk solver used in this study is open source and available at <http://basilisk.fr/>. The specific simulation setup and post-processing scripts for the precursor and two-phase simulations are accessible at the following links: <https://github.com/DeikeLab/precursor> and https://github.com/DeikeLab/turbulent_setup.

Acknowledgments

This work is supported by the *National Science Foundation* under grant 2318816 to LD (Physical Oceanography program), the *NASA Ocean Vector Winds Science Team*, grant 80NSSC23K0983 to LD and JTF. NS was supported by the fellowship *High Meadows Environmental Institute Postdoctoral Teaching Program*. Computations were performed using the *Stellar* machine, granted by the *Cooperative Institute for Earth System modeling* (CIMES), and managed by Princeton Research Computing. This includes the Princeton Institute for Computational Science and Engineering, the Office of Information Technology's High-Performance Computing Center, and the Visualization Laboratory at Princeton University. NS acknowledges the discussion with Alexander Babanin during the WISE Meeting 2025.

References

- Banner, M. L. and Peirson, W. L. (1998). Tangential stress beneath wind-driven air–water interfaces. *Journal of Fluid Mechanics*, 364:115–145.
- Banner, M. L. and Peirson, W. L. (2007). Wave breaking onset and strength for two-dimensional deep-water wave groups. *Journal of Fluid Mechanics*, 585:93–115.
- Belcher, S. E. (1999). Wave growth by non-separated sheltering. *European Journal of Mechanics-B/Fluids*, 18(3):447–462.
- Belcher, S. E. and Hunt, J. C. R. (1993). Turbulent shear flow over slowly moving waves. *Journal of Fluid Mechanics*, 251:109–148.
- Buckley, M. P., Veron, F., and Yousefi, K. (2020). Surface viscous stress over wind-driven waves with intermittent airflow separation. *Journal of Fluid Mechanics*, 905:A31.
- Craig, P. D. and Banner, M. L. (1994). Modeling wave-enhanced turbulence in the ocean surface layer. *Journal of Physical Oceanography*, 24(12):2546–2559.
- De Vita, F., Verzicco, R., and Iafrati, A. (2018). Breaking of modulated wave groups: kinematics and energy dissipation processes. *Journal of Fluid Mechanics*, 855:267–298.
- Deike, L. (2022). Mass transfer at the ocean–atmosphere interface: the role of wave breaking, droplets, and bubbles. *Annual Review of Fluid Mechanics*, 54:191–224.
- Deike, L., Melville, W. K., and Popinet, S. (2016). Air entrainment and bubble statistics in breaking waves. *Journal of Fluid Mechanics*, 801:91–129.
- Deike, L., Popinet, S., and Melville, W. K. (2015). Capillary effects on wave breaking. *Journal of Fluid Mechanics*, 769:541–569.
- Donelan, M. A., Babanin, A. V., Young, I. R., and Banner, M. L. (2006). Wave-follower field measurements of the wind-input spectral function. part ii: Parameterization of the wind input. *Journal of Physical Oceanography*, 36(8):1672–1689.
- Drazen, D. A., Melville, W. K., and Lenain, L. (2008). Inertial scaling of dissipation in unsteady breaking waves. *Journal of Fluid Mechanics*, 611:307–332.

- Drennan, W. M., Donelan, M. A., Terray, E. A., and Katsaros, K. B. (1996). Oceanic turbulence dissipation measurements in swade. *Journal of Physical Oceanography*, 26(5):808–815.
- Duncan, J. H. (1981). An experimental investigation of breaking waves produced by a towed hydrofoil. *Proceedings of the Royal Society of London. A. Mathematical and Physical Sciences*, 377(1770):331–348.
- Gemmrich, J., Mudge, T., and Polonichko, V. (1994). On the energy input from wind to surface waves. *Journal of Physical Oceanography*, 24(11):2413–2417.
- Grare, L., Peirson, W. L., Branger, H., Walker, J. W., Giovanangeli, J. P., and Makin, V. (2013). Growth and dissipation of wind-forced, deep-water waves. *Journal of Fluid Mechanics*, 722:5–50.
- Grare, L., Lenain, L., M. (2013). Wave-coherent airflow and critical layers over ocean waves. *Journal of Physical Oceanography*, 43(10):2156–2172.
- Iafrati, A. (2009). Numerical study of the effects of the breaking intensity on wave breaking flows. *Journal of Fluid Mechanics*, 622:371–411.
- Janssen, P. (2004). *The interaction of ocean waves and wind*. Cambridge University Press.
- Jeffreys, H. (1925). On the formation of water waves by wind. *Proceedings of the Royal Society of London. Series A, Containing Papers of a Mathematical and Physical Character*, 107(742):189–206.
- Kihara, N., Hanazaki, H., Mizuya, T., and Ueda, H. (2007). Relationship between airflow at the critical height and momentum transfer to the traveling waves. *Physics of Fluids*, 19(1).
- Kudryavtsev, V. and Chapron, B. (2016). On growth rate of wind waves: impact of short-scale breaking modulations. *Journal of Physical Oceanography*, 46(1):349–360.
- Lamarre, E. and Melville, W. K. (1991). Air entrainment and dissipation in breaking waves. *Nature*, 351(6326):469–472.
- Lamb, S. H. (1993). *Hydrodynamics*. Cambridge University Press, London, 6th edition.
- Li, T. and Shen, L. (2022). The principal stage in wind-wave generation. *Journal of Fluid Mechanics*, 934:A41.
- Melville, W. K. (1994). Energy dissipation by breaking waves. *Journal of Physical Oceanography*, 24(10):2041–2049.
- Melville, W. K. (1996). The role of surface-wave breaking in air-sea interaction. *Annual Review of Fluid Mechanics*, 28(1):279–321.
- Melville, W. K. and Fedorov, A. V. (2015). The equilibrium dynamics and statistics of gravity-capillary waves. *Journal of Fluid Mechanics*, 767:449–466.
- Melville, W. K. and Rapp, R. J. (1985). Momentum flux in breaking waves. *Nature*, 317(6037):514–516.
- Miles, J. (1957). On the generation of surface waves by shear flows. *Journal of Fluid Mechanics*, 3(2):185–204.
- Miles, J. (1959). On the generation of surface waves by shear flows. part 2. *Journal of Fluid Mechanics*, 6(4):568–582.
- Mostert, W., Popinet, S., and Deike, L. (2022). High-resolution direct simulation of deep water breaking waves: transition to turbulence, bubbles and droplets production. *Journal of Fluid Mechanics*, 942:A27.
- Peirson, W. L. and Garcia, A. W. (2008). On the wind-induced growth of slow water waves of finite steepness. *Journal of Fluid Mechanics*, 608:243–274.
- Perlin, M., Choi, W., and Tian, Z. (2013). Breaking waves in deep and intermediate waters. *Annual review of fluid mechanics*, 45(1):115–145.
- Perrard, S., Lozano-Durán, A., Rabaud, M., Benzaquen, M., and Moisy, F. (2019). Turbulent wind-print on a liquid surface. *Journal of Fluid Mechanics*, 873:1020–1054.
- Phillips, O. M. (1957). On the generation of waves by turbulent wind. *Journal of Fluid Mechanics*, 2(5):417–445.
- Phillips, O. M. (1985). Spectral and statistical properties of the equilibrium range in wind-generated gravity waves. *Journal of Fluid Mechanics*, 156:505–531.
- Pizzo, N. E. and Melville, W. K. (2013). Vortex generation by deep-water breaking waves. *Journal of Fluid Mechanics*, 734:198–218.
- Plant, W. J. (1982). A relationship between wind stress and wave slope. *Journal of Geophysical Research: Oceans*, 87(C3):1961–1967.
- Pollard, R. (1973). Interpretation of near-surface current meter observations. In *Deep Sea Research and Oceanographic Abstracts*, volume 20, pages 261–268. Elsevier.

- Popinet, S. (2015). A quadtree-adaptive multigrid solver for the serre–green–naghdi equations. *Journal of Computational Physics*, 302:336–358.
- Popinet, S. (2018). Numerical models of surface tension. *Annual Review of Fluid Mechanics*, 50:49–75.
- Romero, L., Melville, W. K., and Kleiss, J. M. (2012). Spectral energy dissipation due to surface wave breaking. *Journal of Physical Oceanography*, 42(9):1421–1444.
- Scapin, N., Wu, J., Farrar, J. T., B., C., Popinet, S., and Deike, L. (2025). Momentum fluxes in wind-forced breaking waves. *Journal of Fluid Mechanics*, 1009:A20.
- Snyder, R. L., Dobson, F. W., Elliott, J. A., and Long, R. B. (1981). Oceanic wave growth and the air-sea momentum transfer. *Boundary-Layer Meteorology*, 21(1):101–132.
- Sroka, S. and Emanuel, K. (2021). A review of parameterizations for enthalpy and momentum fluxes from sea spray in tropical cyclones. *Journal of Physical Oceanography*, 51(10):3053–3069.
- Sullivan, P. P. and McWilliams, J. C. (2010). Dynamics of winds and currents coupled to surface waves. *Annual Review of Fluid Mechanics*, 42:19–42.
- Sutherland, P. and Melville, W. K. (2015). Field measurements of surface and near-surface turbulence in the presence of breaking waves. *Journal of Physical Oceanography*, 45(4):943–965.
- Taylor, G. I. (1938). The spectrum of turbulence. *Proceedings of the Royal Society of London. Series A-Mathematical and Physical Sciences*, 164(919):476–490.
- Terray, E. A., Donelan, M., Agrawal, Y., Drennan, W., Kahma, K., Williams, A. J., Hwang, P., and Kitaigorodskii, S. (1996). Estimates of kinetic energy dissipation under breaking waves. *Journal of Physical Oceanography*, 26(5):792–807.
- Thomson, J., Schwendeman, M. S., Zippel, S. F., Moghimi, S., Gemmrich, J., and Rogers, W. E. (2016). Wave-breaking turbulence in the ocean surface layer. *Journal of Physical Oceanography*, 46(6):1857–1870.
- Townsend, A. A. (1951). The structure of the turbulent boundary layer. In *Mathematical Proceedings of the Cambridge Philosophical Society*, volume 47, pages 375–395. Cambridge University Press.
- Van Hooft, J. A., Popinet, S., Van Heerwaarden, C. C., Van der Linden, S. J. A., De Roode, S. R., and Van de Wiel, B. J. H. (2018). Towards adaptive grids for atmospheric boundary-layer simulations. *Boundary-Layer Meteorology*, 167:421–443.
- Vassilicos, J. C. (2015). Dissipation in turbulent flows. *Annual Review of Fluid Mechanics*, 47:95–114.
- Veron, F. and Melville, W. K. (2001). Experiments on the stability and transition of wind-driven water surfaces. *Journal of Fluid Mechanics*, 446:25–65.
- Wu, H.-Y., Hsu, E.-Y., and Street, R. L. (1979). Experimental study of nonlinear wave—wave interaction and white-cap dissipation of wind-generated waves. *Dynamics of Atmospheres and Oceans*, 3(1):55–78.
- Wu, J. and Deike, L. (2021). Wind wave growth in the viscous regime. *Physical Review Fluids*, 6(9):094801.
- Wu, J., Popinet, S., Chapron, B., Farrar, J. T., and Deike, L. (2025). Turbulence and energy dissipation from wave breaking. *arXiv preprint arXiv:2503.03009*.
- Wu, J., Popinet, S., and Deike, L. (2022). Revisiting wind wave growth with fully coupled direct numerical simulations. *Journal of Fluid Mechanics*, 951:A18.
- Wu, J., Popinet, S., and Deike, L. (2023). Breaking wave field statistics with a multi-layer model. *Journal of Fluid Mechanics*, 968:A12.
- Yang, D., Meneveau, C., and Shen, L. (2013). Dynamic modelling of sea-surface roughness for large-eddy simulation of wind over ocean wavefield. *Journal of Fluid Mechanics*, 726:62–99.
- Zippel, S. F., Farrar, J. T., Zappa, C. J., and Plueddemann, A. J. (2022). Parsing the kinetic energy budget of the ocean surface mixed layer. *Geophysical Research Letters*, 49(2):e2021GL095920.
- Zippel, S. F., Maksym, T., Scully, M., Sutherland, P., and Dumont, D. (2020). Measurements of enhanced near-surface turbulence under windrows. *Journal of Physical Oceanography*, 50(1):197–215.

Supplementary Material

Growth and dissipation in wind-forced breaking waves

Nicolò Scapin^{1,2}, Jiarong Wu^{1,3}, J. Thomas Farrar⁴, Bertrand Chapron⁵, Stéphane Popinet⁶,
and Luc Deike^{1,2}

¹Department of Mechanical and Aerospace Engineering, Princeton University, Princeton,
NJ 08544, USA

²High Meadows Environmental Institute, Princeton University, Princeton, NJ 08544, USA

³Courant Institute of Mathematical Sciences, New York University, US

⁴Woods Hole Oceanographic Institution (WHOI)

⁵IFREMER, Univ. Brest, CNRS, IRD, LOPS, France

⁶Institut Jean Le Rond d'Alembert, CNRS UMR 7190, Sorbonne Université, Paris 75005,
France

1 Methodology: Direct Numerical Simulations

In this section of the supplementary material, we describe the numerical methodology employed to study wind-forced breaking waves in the high wind-speed regime. The main feature of our approach is to treat the system composed of wind, waves, and water as a two-phase system, i.e., air and water, where the wave field is located at the interface between the two phases, solving for the most general two-phase Navier-Stokes equations without simplifications or subgrid-scale model. A sketch of this configuration is shown in figure 1.

To distinguish the two phases, an indicator function \mathcal{H} is introduced. It is set equal to 0 in the air and to 1 in the water, with a small transition region, i.e. $0 < \mathcal{H} < 1$, corresponding to the wave interface. The evolution of \mathcal{H} and the wave field is governed by the advection equation

$$\frac{\partial \mathcal{H}}{\partial t} + \mathbf{u} \cdot \nabla \mathcal{H} = 0, \quad (1)$$

where $\mathbf{u} = (u, v, w)$ is the three-dimensional velocity field, obtained by solving the incompressible Navier-Stokes equations in both the air and water phases, including surface tension effects. These equations read (Tryggvason et al., 2011):

$$\nabla \cdot \mathbf{u} = 0, \quad (2)$$

$$\frac{\partial(\rho \mathbf{u})}{\partial t} + \nabla \cdot (\rho \mathbf{u} \mathbf{u}) = -\nabla p + \nabla \cdot [\mu(\nabla \mathbf{u} + \nabla \mathbf{u}^T)] + \sigma \kappa \delta_\Gamma \mathbf{n}_\Gamma + \rho g \mathbf{e}_z, \quad (3)$$

where p is the pressure, σ is the surface tension coefficient, g is gravity with $\mathbf{e}_z = (0, 0, -1)$ is a unit vector, κ is the curvature of the interface, \mathbf{n}_Γ is the outward-pointing unit normal to the interface, i.e. the wave field, and δ_Γ is the Dirac distribution which is not zero only at the interface. In equation (3), ρ and μ are the density and dynamic viscosity fields, which are computed using an arithmetic average based on the indicator function as

$$\rho = \rho_w \mathcal{H} + \rho_a (1 - \mathcal{H}), \quad (4)$$

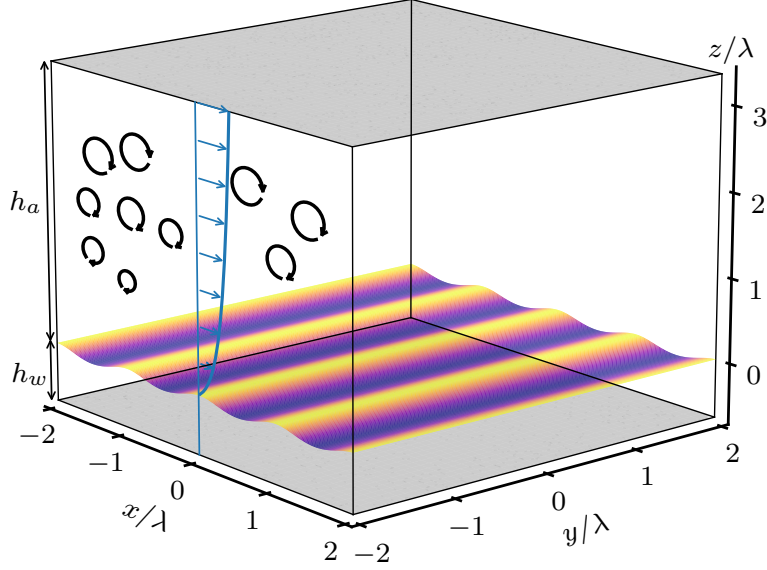


Figure 1: Illustration of the system composed of turbulent airflow ($0 \leq z \leq h_a$), the wave field and the water field ($-h_w \leq z \leq 0$). Here, h_a and h_w are the mean air and water mean heights with λ the fundamental wavelength. The airflow is a fully developed turbulent boundary layer (mean profile in light-blue line, while turbulent eddies are illustrated in black). In the surface contour, dark-purple regions denote wave troughs, while yellow regions indicate wave crests.

$$\mu = \mu_w \mathcal{H} + \mu_a (1 - \mathcal{H}), \quad (5)$$

where subscripts w and a denote the water and air properties, respectively.

Equations (1), (2), and (3) are solved using state-of-the-art numerical methods for multiphase flow implemented in the open-source Basilisk solver¹; see e.g. (Popinet, 2015, 2018; Van Hooft et al., 2018) for more details. In particular, equation (1) is solved using a conservative and diffusion-free geometric volume-of-fluid method, which enables accurate reconstruction and advection of the interface between the air and water phases. Equations (2) and (3) are solved using a pressure-correction scheme: the velocity is first predicted without including the pressure gradient, and then corrected to enforce the divergence-free condition in equation (2). Furthermore, the momentum equation is discretized using a momentum-conserving scheme, which ensures numerical stability even in the presence of high-density ratios, such as those encountered in air–water systems. The entire set of equations is solved on an adaptive grid, providing high resolution near the wave field while maintaining a coarser mesh in the bulk of each phase.

The key advantage of this approach is that it does not require any model for wave motion or subgrid-scale turbulence, thereby enabling a realistic, first-principles description of the coupling among wind, the wave field, and water currents. We use adaptive mesh refinement, allowing us to resolve the spatial and temporal scales of wind, current, and wave breaking from $\mathcal{O}(10^{-3})$ m to $\mathcal{O}(10^0)$ m. Such numerical methodology for two-phase flows, as implemented in Basilisk, has been successfully applied to a range of turbulent two-phase processes, including drops and bubbles in turbulence (Riviere et al., 2021; Perrard et al., 2021; Farsoiyya et al., 2023), wave breaking (Deike et al., 2016; Mostert et al., 2022), the atmospheric boundary layer (Van Hooft et al., 2018), and wind-driven wave growth (Wu & Deike, 2021; Wu et al., 2022). Here, we extend this framework to wind-forced breaking waves, building on our previous work on momentum fluxes (Scapin et al., 2025).

¹<http://basilisk.fr/>

2 Set-up and summary of the simulated cases

In this section, we recall the two main simulation steps, described in Wu et al. (2022); Scapin et al. (2025) and we provide a summary of the different simulated cases.

2.1 Initialization and precursor

The simulations are conducted in two steps: the generation of the precursor air-side turbulent field and the actual two-phase simulation resolving for the coupled wind, waves, and current.

First, we initialize the airflow region using a fully developed turbulent flow field at the desired friction Reynolds number, $Re_{*,\lambda}$, following Wu et al. (2022); Scapin et al. (2025). This initialization involves a precursor simulation conducted independently in a single-phase setup and employing the same domain. During this precursor simulation, the wave field with profile η_0 remains at rest, and a no-slip/no-penetration boundary condition is enforced on the wave surface for the velocity field, using the embedded boundary method (Johansen & Colella, 1998) available within the Basilisk framework (Ghigo et al., 2021). The precursor simulation is performed long enough until the turbulent airflow achieves a statistically steady state by adding an external body force per unit mass acting in the streamwise direction, i.e. $\partial p_0 / \partial x (1 - \mathcal{H}) \mathbf{e}_x$ with $\mathbf{e}_x = (1, 0, 0)$, on the right-hand side of the momentum equation (3). In the expression of the body force, $\partial p_0 / \partial x$ is a uniform pressure gradient driving the flow and, here, reads as

$$\frac{\partial p_0}{\partial x} = \frac{\rho_a u_*^2}{h_a}. \quad (6)$$

The imposed pressure gradient sets the nominal friction velocity u_* and prescribes the total stress $\rho_a u_*^2$ on the wave field. Once a statistically steady state is achieved for the precursor, the resulting fully developed turbulent field is employed as an initial condition for the airflow region in the two-phase simulations.

The second step involves initializing the water orbital velocity using the third-order potential flow solution obtained for a third-order Stokes wave. After the two-phase simulation begins, the airflow and wave field dynamically evolve without any prescribed conditions at the two-phase interface.

2.2 Summary of the simulated cases

In table 1, we report the different simulated cases with the corresponding dimensionless numbers for each case. Note that the numerical grid in the simulations is adaptive, featuring a minimum grid size $\Delta = L_0 / (2^{Le})$, where Le represents the maximum level of refinement. The Adaptive Mesh Refinement (AMR) technique significantly reduces computational costs by maintaining a highly refined grid near the interface and in the boundary layers while allowing coarser grids in the bulk airflow, provided that refinement criteria are met (Popinet, 2015; Van Hooft et al., 2018). Following Wu et al. (2022); Scapin et al. (2025), the refinement criteria for the air and water velocity components and the volume fraction are set equal to $\epsilon_{ua} = 0.3u_*$, $\epsilon_{uw} = 10^{-3}c$ and $\epsilon_{\mathcal{F}} = 10^{-4}$, respectively.

The computational costs of these simulations include generating a precursor simulation and running the two-phase simulations. Four precursors are used for varying air-side Reynolds number ($Re_{*,\lambda} = 53.5 - 107 - 214$) and the ratio $h_a / \lambda = 3.36 - 6.72$, amounting to $\approx 1.5 \cdot 10^5$ CPU each. Each two-phase simulation at $Le = 10$ requires $\approx 4.2 \cdot 10^5$ CPU hours, while the two simulations at $Le = 11$ require $\approx 1.20 \cdot 10^6$ CPU hours each. We employ 384 processors for the precursor simulations and for the two-phase cases 480 at $Le = 10$, and 980 processors at $Le = 11$. The total cost of the simulation campaign is about $6 \cdot 10^6$ CPU hours.

u_*/c	$Re_{*,\lambda}$	Re_W	μ_w/μ_a	h_a/λ	Le	CPU hours
0.30	214	$2.55 \cdot 10^4$	22.84	3.36	10	$4.2 \cdot 10^5$
0.40	214	$2.55 \cdot 10^4$	17.13	3.36	10	$4.2 \cdot 10^5$
0.50	214	$2.55 \cdot 10^4$	13.71	3.36	10	$4.2 \cdot 10^5$
0.70	214	$2.55 \cdot 10^4$	9.79	3.36	10	$4.2 \cdot 10^5$
0.90	214	$2.55 \cdot 10^4$	7.61	3.36	10	$4.2 \cdot 10^5$
0.90	53.5	$2.55 \cdot 10^4$	1.90	3.36	10	$4.2 \cdot 10^5$
0.90	107	$2.55 \cdot 10^4$	3.81	3.36	10	$4.2 \cdot 10^5$
0.90	214	$2.55 \cdot 10^4$	7.61	3.36	11	$1.2 \cdot 10^6$
0.90	107	$2.55 \cdot 10^4$	3.81	6.72	11	$1.2 \cdot 10^6$

Table 1: Summary of the simulated cases for different values of u_*/c . In the table, $Re_{*,\lambda} = \rho_a u_* \lambda / \mu_a$, $Re_W = \rho_w c \lambda / \mu_w$, μ_w / μ_a and h_a / λ . The cases with $h_a / \lambda = 3.36$ correspond to 4 waves per box size, whereas the case with $h_a / \lambda = 6.72$ to 8 waves per box size. For the different cases, the initial steepness is set equal to $a_0 k = 0.3$, and the density ratio is taken as $\rho_w / \rho_a = 816$ and the Bond number $Bo = 200$.

3 A note on the wall-layer scaling for the underwater dissipation

We briefly summarize why the physical argument behind modeling dissipation using a wall-layer turbulence model is not appropriate for the underwater dissipation due to wave breaking. The wall-layer model assumes a balance between turbulence production by mean shear and its dissipation, as is typical in a turbulent boundary layer. Applying a logarithmic velocity profile leads to the following expression for the turbulence dissipation rate:

$$\langle \varepsilon \rangle_{wl}(z) = \frac{u_{*,w}^3}{\kappa z}, \quad (7)$$

where $u_{*,w}$ is the friction velocity in water, and $\kappa = 0.41$ is the von Kármán constant. Following Terray et al. (1996), $u_{*,w}$ is estimated as $u_{*,w} = u_*(\rho_a / \rho_w)^{1/2}$, assuming that the total stress in the air is fully transferred to the water side.

We test the wall-layer scaling using the dissipation profiles from the second growth cycle but find that it fails to collapse the cases for different values of u_*/c , as clearly shown by figure 2(a). This discrepancy arises because the assumed production-dissipation balance is disrupted by wave breaking, which substantially enhances turbulence dissipation compared to the estimate of equation (7). This enhancement has been demonstrated in several previous studies (Craig & Banner, 1994; Gemmrich et al., 1994; Terray et al., 1996; Sutherland & Melville, 2015; Zippel et al., 2020) and is also demonstrated in figure 3 of the main text.

A more physically representative scaling is derived in the main text, based on the energy dissipation due to breaking $S_{ds} = \rho_w g^{-1} L_c^{-1} b c^5$, which we repeat in this supplementary in figure 2(b) or based on wind input given the balance between dissipation due to breaking and wind input (shown in main text and repeated in figure 2(c)). We note that a simplified scaling based on wind input can be proposed since the wind input can be approximated as $S_{in} = \rho_a u_*^2 c$ and the vertical profile can be rescaled as

$$\langle \varepsilon \rangle(z) = \tilde{A} \frac{\rho_a}{\rho_w} \frac{u_*^2 c}{z}, \quad (8)$$

where $\tilde{A} \approx 0.16$ is a non-dimensional constant obtained by best fit to the data. This value is very similar to the constant A used in figure 2(c) for the group $\rho_w \langle \varepsilon \rangle(z) H_s / S_{in}$ and to the constant \mathcal{A} used in figure 2(b) for the group $\langle \varepsilon \rangle(z) / (|g|^{-1} L_c^{-1} b c^5)$. Note that equation (8) incorporates the effects of

both the friction velocity u_* and the wave phase speed c . Figure 2(d) shows the dissipation profiles

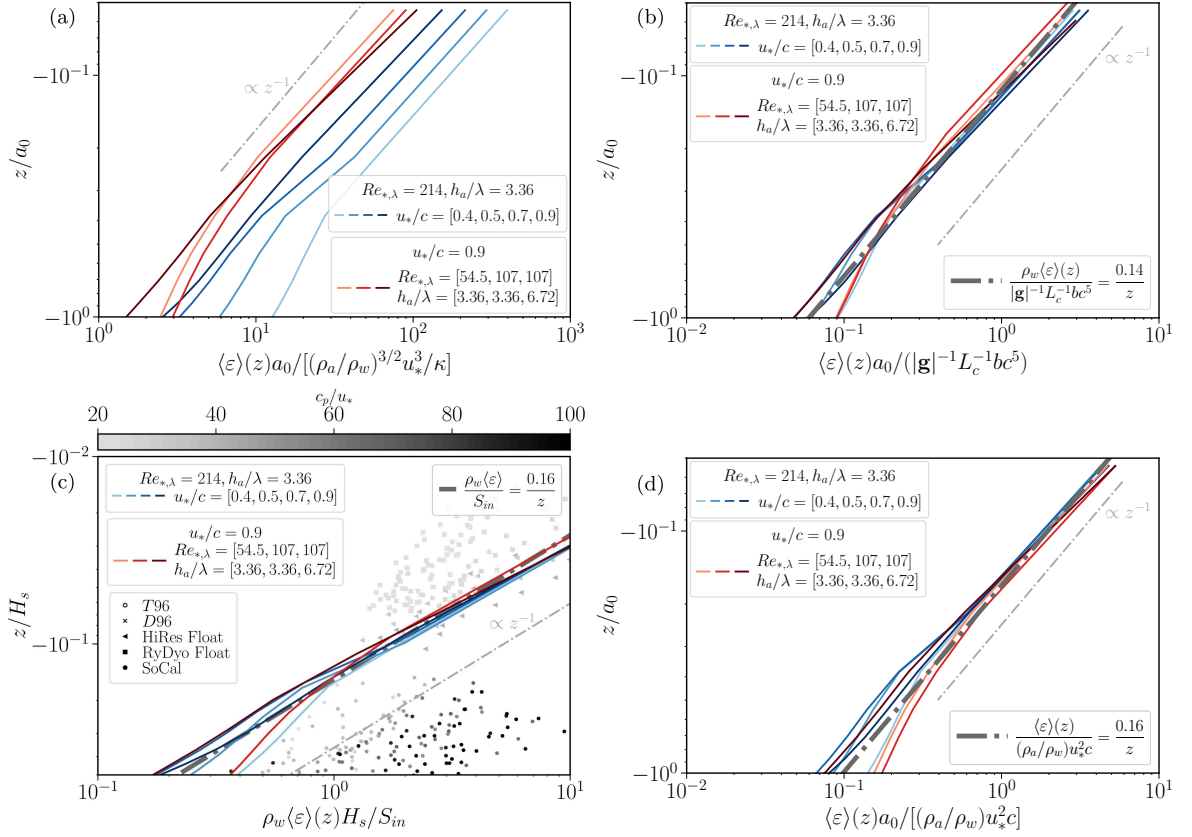


Figure 2: Dissipation profiles after breaking (G_2), normalized by: (a) wall-layer scaling $(\rho_a/\rho_w)^{3/2}u_*^3/(\kappa a_0)$, (b) the dissipation-based scaling $S_{ds}/(\rho_w a_0)$ with $S_{ds} = \rho_w g^{-1} L_c^{-1} b c^5$, (c) the wind input S_{in} , which is extracted from the DNS in the present work, while in Terray et al. (1996); Drennan et al. (1996); Sutherland & Melville (2015), it is computed using a spectral parametrization, (d) wind-input scaling $(\rho_a/\rho_w)u_*^2 c/a_0$. In (a)-(b)-(d), the depth is normalized by the initial amplitude a_0 , in (c) by the significant wave height H_s to compare with field data (Terray et al., 1996; Drennan et al., 1996; Sutherland & Melville, 2015).

normalized using the scaling in equation (8), revealing excellent collapse within a water depth of $5a_0$ for a range of u_*/c and $Re_{*,\lambda}$ values.

It is important to emphasize that the scaling in equation (8) is fully consistent with the dissipation-based scaling in equation 14 of the main text, given the balance between wind input S_{in} and energy dissipation S_{ds} .

References

- Craig, P. D., & Banner, M. L. (1994). Modeling wave-enhanced turbulence in the ocean surface layer. *Journal of Physical Oceanography*, 24(12), 2546–2559. doi: 10.1175/1520-0485(1994)
- Deike, L., Melville, W. K., & Popinet, S. (2016). Air entrainment and bubble statistics in breaking waves. *Journal of Fluid Mechanics*, 801, 91–129.
- Drennan, W. M., Donelan, M. A., Terray, E. A., & Katsaros, K. B. (1996). Oceanic turbulence dissipation measurements in swade. *Journal of Physical Oceanography*, 26(5), 808–815. doi: 10.1175/1520-0485(1996)

- Farsoiyya, P. K., Liu, Z., Daiss, A., Fox, R. O., & Deike, L. (2023). Role of viscosity in turbulent drop break-up. *Journal of Fluid Mechanics*, 972, A11.
- Gemmrich, J. R., Mudge, T. D., & Polonichko, V. D. (1994). On the energy input from wind to surface waves. *Journal of Physical Oceanography*, 24(11), 2413–2417. doi: 10.1175/1520-0485(1994)
- Ghigo, A. R., Popinet, S., & Wachs, A. (2021). A conservative finite volume cut-cell method on an adaptive cartesian tree grid for moving rigid bodies in incompressible flows.
- Johansen, H., & Colella, P. (1998). A cartesian grid embedded boundary method for poisson’s equation on irregular domains. *Journal of Computational Physics*, 147(1), 60–85.
- Mostert, W., Popinet, S., & Deike, L. (2022). High-resolution direct simulation of deep water breaking waves: transition to turbulence, bubbles and droplets production. *Journal of Fluid Mechanics*, 942, A27.
- Perrard, S., Rivière, A., Mostert, W., & Deike, L. (2021). Bubble deformation by a turbulent flow. *Journal of Fluid Mechanics*, 920, A15.
- Popinet, S. (2015). A quadtree-adaptive multigrid solver for the serre–green–naghdi equations. *Journal of Computational Physics*, 302, 336–358.
- Popinet, S. (2018). Numerical models of surface tension. *Annual Review of Fluid Mechanics*, 50, 49–75.
- Riviere, A., Mostert, W., Perrard, S., & Deike, L. (2021). Sub-hinze scale bubble production in turbulent bubble break-up. *Journal of Fluid Mechanics*, 917, A40.
- Scapin, N., Wu, J., Farrar, J. T., B., C., Popinet, S., & Deike, L. (2025). Momentum fluxes in wind-forced breaking waves. *Journal of Fluid Mechanics*, 1009, A20. doi: 10.1017/jfm.2025.77
- Sutherland, P., & Melville, W. K. (2015). Field measurements of surface and near-surface turbulence in the presence of breaking waves. *Journal of Physical Oceanography*, 45(4), 943–965. doi: 10.1175/JPO-D-14-0133.1
- Terray, E. A., Donelan, M. A., Agrawal, Y. C., Drennan, W. M., Kahma, K. K., Williams, A. J. I., ... Kitaigorodskii, S. A. (1996). Estimates of kinetic energy dissipation under breaking waves. *Journal of Physical Oceanography*, 26(5), 792–807. doi: 10.1175/1520-0485(1996)
- Tryggvason, G., Scardovelli, R., & Zaleski, S. (2011). *Direct numerical simulations of gas–liquid multiphase flows*. Cambridge University Press.
- Van Hooft, J. A., Popinet, S., Van Heerwaarden, C. C., Van der Linden, S. J. A., De Roode, S. R., & Van de Wiel, B. J. H. (2018). Towards adaptive grids for atmospheric boundary-layer simulations. *Boundary-Layer Meteorology*, 167, 421–443.
- Wu, J., & Deike, L. (2021). Wind wave growth in the viscous regime. *Physical Review Fluids*, 6(9), 094801.
- Wu, J., Popinet, S., & Deike, L. (2022). Revisiting wind wave growth with fully coupled direct numerical simulations. *Journal of Fluid Mechanics*, 951, A18.
- Zippel, S. F., Maksym, T., Scully, M., Sutherland, P., & Dumont, D. (2020). Measurements of enhanced near-surface turbulence under windrows. *Journal of Physical Oceanography*, 50(1), 197–215. doi: 10.1175/JPO-D-19-0043.1